Revised Manuscript - clean version Click here to view linked References

Microstructure evolution by thermomechanical processing and high-temperature mechanical properties of HCP-high entropy alloys (HEAs)

S.J.Liang [a], S. Matsunaga [a], Y. Toda [b], Y. Yamabe-Mitarai [a*]

[a] Department of Advanced Materials Science, Graduate School of Frontier Sciences, The University of Tokyo, 5-1-5 Kashiwanoha, Kashiwa City, Chiba 277-8561, Japan

[b] National Institute for Materials Science, 1-2-1 Sengen, Tsukuba, Ibaraki, 305-0047, Japan

[*]Corresponding authors' email: mitarai.yoko@edu.k.u-tokyo.ac.jp

Keywords: HCP-HEAs, Thermomechanical processing, Equiaxed HCP phase, High temperature strength, Deformation mechanism

Abstract

The solid solution strengthening and deformation mechanisms of the hcp-high entropy alloys (HEAs) have not been elucidated yet because of the complexity introduced by the martensite structure, particularly in alloys undergoing phase transformation from bcc to hcp structures. This study attempted to fabricate an equiaxed hcp microstructure for TiZrHf, TiZrHfAl, and TiZrHfAlSc using the hot rolling process and subsequent heat treatment. The equiaxed hcp phase was successfully formed in TiZrHfAl, but the martensite structure remained in TiZrHf and TiZrHfAlSc. The 0.2 % proof stress at 400 and 600°C increased with the increase of the average atomic size misfit δ and the mixing entropy ΔS_{mix}. The low activation volume and high-stress exponent of TiZrHfAl with equiaxed hcp phase at room temperature suggest minor obstacles such as cluster or short-range order inhibit the movement of dislocation and leading to the significant solid-solution strengthening. However, the effect diminished at 600 °C.

1. Introduction

High-temperature (HT)-titanium alloys are widely used as heat-resistant materials in fan blades and compressor components of aircraft jet engines, due to their lightweight, excellent strength, and other corrosion resistance at high temperatures [1,2]. Despite their lightweight, excellent strength, and high-temperature corrosion resistance, the applications of current high-temperature (HT) titanium alloys are limited by their degradation in mechanical properties such as high-temperature strength, fatigue strength, creep, and oxidation resistance, especially when exposed to environments above 600°C

[3]. These properties are critical for jet engine applications, where exposure to high temperatures is required. Hence, developing advanced HT-titanium alloys is necessary to improve heat resistance, which can withstand extreme conditions while maintaining their mechanical properties. However, the demands for higher operating temperatures and improved mechanical properties have led to exploring alternative high-temperature materials, including high-entropy alloys (HEAs) [4].

HEAs represent a unique class of materials consisting of multiple elements with near-equiatomic composition and high configurational entropy of their constituent elements [4]. These fascinating materials have attracted significant interest in recent years due to their potential to exhibit superior mechanical properties compared to conventional alloys. This is attributed to their specific strengthening mechanism [5]. By incorporating multiple elements into the alloy, the solid solution strengthening effect can be enhanced, which may lead to improved high-temperature strength and stability [6]. Therefore, hcp-HEAs are also expected to improve the solid solution strengthening of current high-temperature alloys such as hcp-Ti alloys. However, the published research on HEAs has mainly concentrated on fcc-type alloys such as CoCrFeNi [7] CoCrFeMnNi [8], AlCoCrFeNi [9], and bcc-type alloys like NbMoTaVW [10], WTaFeCrV [11], HfNbTaTiZr [12]. The research on the mechanical properties of the hcp-HEAs is limited [6].

In recent years, several studies have reported the successful fabrication of hcp-HEAs. Initially, Takeuchi et al. [13],reported that nearly single hcp structures formed in YGdTbDyLu and GdTbDyTmLu equiatomic alloys. However, the practical use of these alloys is limited due to their high dependence on rare earth elements. Subsequently, a growing number of hcp-TiZrHf HEAs have been reported, taking into account the practical applications, for instance, TiZrHf [14–16], TiZrHfSc [14],[16],[17],[18], TiZrHfY [14], AlHfScTiZr [19], TiZrHfYLa [20], ScYLaTiZrHf [21], ScTiZrHfRe [22]. What's more, despite some prior reports indicating that TiZrHfAl alloys formed a bcc and 194-Zr_2Al phases [16],[23], the calculated phase diagrams for TiZrHfAl reported by Nagase et al. [23], clearly indicate the hcp phase region in the temperature range below 1400 K. Consequently, the possibility of forming a stable hcp structure through heat treatment in this temperature range is expected in TiZrHfAl. Based on these results, it can be inferred that adding hcp-stabilizing elements such as Sc, Al, and Y to TiZrHf-based alloys significantly stabilizes the hcp structure in HEAs.

These hcp-HEAs exhibit excellent mechanical properties. Huang et al., reported that TiZrHf exhibited a yield strength of 773 MPa, whereas TiZrHfSc and TiZrHfY exhibited a yield strength of 1001 and 554 MPa at room temperature, respectively [14]. This is because Sc is solid-solution in TiZrHf, but Y is not solid-solution in TiZrHf and Y exists

interdendritic area between TiZrHf dendrite. Ł. Rogal et al. reported the strength of TiZrHfScAl at room temperature was 1450 MPa [19]. Gan et al. reported that controlling the ratio of Sc and Al in $Ti_{25}Zr_{25}Hf_{25}Sc_{(25-x)}Al_x$ had a certain effect on enhancing strength and improving ductility [24]. However, among the limited research results available for hcp-HEAs, the results focused on the martensite structure formed when the high-temperature bcc phase transforms into the low-temperature hcp phase [14–16,19]. These specific martensite structures present a barrier to fully understanding the solid solution strengthening and deformation mechanisms in hcp-HEAs. This is primarily due to their inherently high strength, coupled with complex deformation behaviors, which complicates this understanding. Consequently, isolating the influence of microstructure is crucial for an effective analysis of solid solution-strengthening mechanisms in hcp-HEAs. In this context, it becomes indispensable to form equiaxed hcp phases.

Therefore, in this study, we aim to form an equiaxed hcp structure in HEAs, utilizing thermomechanical processing and subsequent heat treatment. TiZrHf, TiZrHfAl, and TiZrHfAlSc alloys, which stabilize the hcp structure, were selected and attempted the formation of the equiaxed hcp phase by thermomechanical processing. The mechanical properties of the obtained microstructure were investigated. Furthermore, a detailed investigation was also conducted to elucidate the solid solution strengthening mechanism of the TiZrHfAl alloy, which possesses an equiaxed hcp structure.

2. Experimental procedure

2.1 Alloy design

TiZrHf, TiZrHfAl, and TiZrHfAlSc were selected to form an equiaxed hcp structure. In the previous study, it was observed that the TiZrHfAl formed Zr_2Al precipitates in the matrix. To inhibit the formation of precipitates, the composition of the matrix phase obtained in the previous study, $Ti_{29}Zr_{23}Hf_{27}Al_{21}$ [16], was selected as the alloy composition.

The mixing entropy, ΔS_{mix}, is defined by the following equation (1):

$$\Delta S_{mix} = -R \sum_{i=1}^{n} x_i \ln x_i \quad (1)$$

where R is the gas constant (8.314 J/(K·mol)) and x_i is the atomic ratio of the *i-th* element. The average atomic radius misfit δ is defined by the following equation (2):

$$\delta = 100\sqrt{\sum_i x_i \bullet \left(1 - \frac{r_i}{\bar{r}}\right)^2} \quad (2)$$

where the r_i is the atomic radius of *ith* element, and the $\bar{r}$ is the average atomic radius.

The nominal compositions of the alloys are presented in Table 1. The mixing entropy, ΔS_{mix}, the average atomic size misfit, δ, are also summarized in Table 1. According to the strict definition of HEAs, TiZrHf and TiZrHfAl are classified as medium entropy alloys. However, in this study, the wide definition of HEAs is used and we call TiZrHf and TiZrHfAl as HEAs.

Table 1 The alloy composition, the mixing entropy (ΔS_{mix}), the average atomic size misfit (δ) of the tested alloys

Alloy	**Composition (Atom ratio) (%)**					**ΔS (R)**	**δ (%)**
	Ti	Zr	Hf	Al	Sc		
TiZrHf	34	33	33	0	0	1.10	3.99
TiZrHfAl	29	23	27	21	0	1.37	4.70
TiZrHfAlSc	20	20	20	20	20	1.61	5.29

2.2 Alloy preparation

Raw materials of Ti (purity of 99.9%, Furuuchi Chemical), Al (purity of 99.99%, Furuuchi Chemical), Zr (purity of 99.9%, Furuuchi Chemical), Hf (purity of 99.7%, Furuuchi Chemical), Sc (purity of 99.7%, Furuuchi Chemical), were weighed in the appropriate amounts to attain the nominal composition as shown in Table 1. The 20g ingots of the alloys with the nominal composition were prepared in an arc-melting furnace with a water-cooled copper plate under a protective argon atmosphere. The alloys were re-melted 5 times to ensure they were fully homogenized. Each drop shape ingot was 8mm in height and 10mm in diameter. Following this, the ingots were heated to 1000℃ for 5 minutes in an air furnace and subsequently hot-rolled. Each rolling step involved a reduction ratio of 10%, and after each rolling step, the sample was reheated at 1000 ℃ for 5 minutes, culminating in a total reduction in thickness of 55%.

2.3 Heat treatment

To promote the formation of equiaxed hcp phases in the alloys, the heat treatment temperature was decided by thermodynamic calculation using Thermo-Calc© software 2022a with the TCTI3 database. As Sc was not included in the TCTI3 database, the alloys without Sc were calculated and presented in Fig. 1. According to the isothermal sections of the TiZrHf alloy and the phase diagram of the TiZrHfAl, the major potential phases in different temperature regions are summarized in Table 2. The TiZrHf alloy exhibits the single hcp phase at temperatures ranging from 700 to 800 ℃ and the hcp + bcc two phases

at 900℃. The TiZrHfAl alloy also forms the hcp phase between 700 and 1000 ℃, although the Al_2Zr_3 or Al_3Zr_5 phase also forms. Therefore, the heat treatment temperature was decided at the temperature range from 700 to 900 ℃. The 3×3×3 mm sample was cut from the rolled sample and enclosed with Ar gas in a quartz tube to prevent material oxidation during heat treatment. The samples were subjected to heat treatment at temperatures ranging from 700 to 900℃ for 24 or 168 hours, followed by either water quenching or furnace cooling.

2.4 Phase identification

The crystal structure of the heat-treated specimens was identified by X-ray diffraction (XRD). The XRD analysis was performed on the equipment of RIGAKU Smartlab with CuKα-radiation (λ = 0.154 nm) at the 2θ range of 10–90° with a scanning rate of 10°/min and 0.02˚step at room temperature. The PDXL-2 (Rigaku) data analysis software and ICDD PDF-4 international diffraction database were used to determine the crystal structure of the phase.

The heat-treated specimens were embedded in conductive phenolic resin (S60PA-K10, IMT Corporation). These mounted specimens underwent automated polishing using a polishing machine (SP-200, Subtech, Inc.) with a sequence of Grit320, 400, 600, and 800 polishing papers, followed by 9 μm, 3 μm, 1μm polycrystalline diamond with silica suspension, and finally received a final polishing with a 5:1 mixture of colloidal silica and hydrogen peroxide solution. The polishing machine operated at 150 rotations per minute, and a load of 0.5 MPa was applied during each step. The microstructure and phase composition of the alloys were analyzed using field emission scanning electron microscopy (FE-SEM, JEOL, JSM7200F) equipped with an energy-dispersive spectrometer (EDS) and was operated at an accelerating voltage of 20 kV.

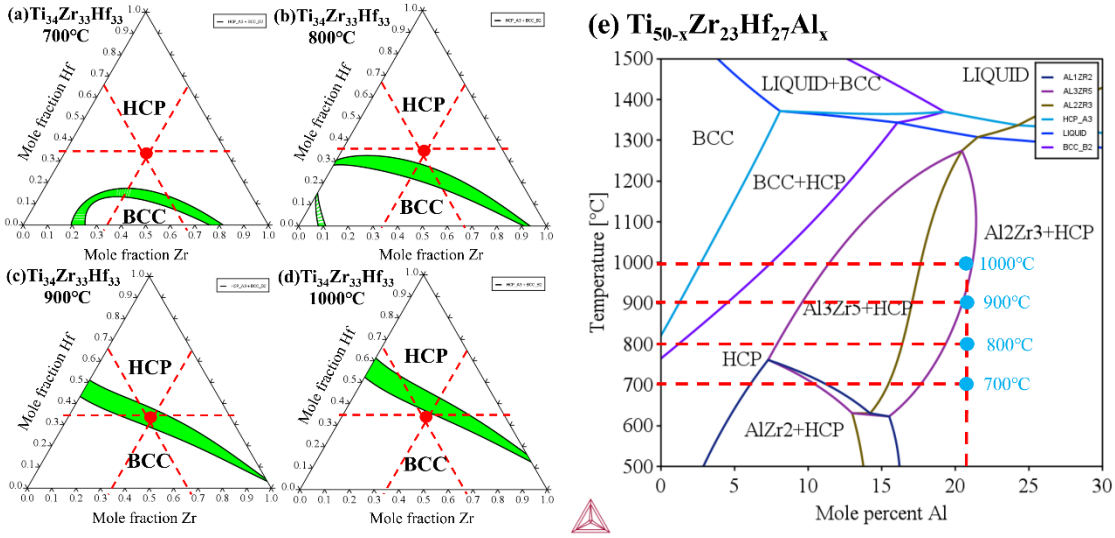


Fig. 1 The isothermal section of TiZrHf at (a) 700℃, (b) 800℃, (c) 900℃, (d) 1000℃, and (e) phase diagram as a function of Al contents of TiZrHfAl.

Table. 2 The stable phase of the calculated by Thermo-Calc software in different temperature regions

Alloy	Temperature region (℃)	The calculated stable phase
TiZrHf	700	hcp
	800	hcp
	900	hcp+bcc
	1000	bcc
TiZrHfAl	700	hcp+Al_2Zr_3
	800	hcp+Al_2Zr_3
	900	hcp+Al_2Zr_3
	1000	hcp+Al_2Zr_3+ Al_3Zr_5

2.5 Evaluation of mechanical properties

To evaluate the 0.2% proof stress, compression tests were performed on heat-treated specimens with dimensions of 3×3×5 mm^3 at 400 and 600 ℃ by using the high-temperature compression testing machine (Shimadzu AG-X). The initial strain rate was set at 3×10^{-4}/s. To investigate the deformation mechanism, strain rate jump tests were carried out on TiZrHfAl at room temperature and 600 ℃, employing strain rates of 3×10^{-5}/s, 3×10^{-4}/s, and 3×10^{-3}/s, respectively. At each step, the strain rate was maintained until 1-5% plastic strain was obtained, then moved to the next step.

3. Results

3.1 Phase analysis and microstructure

Fig. 2 displays the microstructure and Table 3 summarises the EDS chemical analysis results of the as-rolled specimens. In the TiZrHf alloy, martensite structures measuring 2-3 μm in width were observed (Fig. 2(a-1)), while the TiZrHfAlSc alloy exhibited finer martensite structures with widths of less than 1 μm, along with a finer dark equiaxed phase (Fig. 2(c-1)). These martensite structures are consistent with those observed in as-cast specimens in other studies [15,19]. Additionally, elliptical black regions of approximately 1 μm in width were observed in the TiZrHfAlSc alloy as marked in Fig. 2(c). The high concentration of Sc and O in these regions suggests they are likely oxides of Sc, possibly introduced during the rolling process under atmospheric conditions. The elemental distribution within the fine martensite and equiaxed structures in the matrix did not show significant differences.

Most notably, the TiZrHfAl alloy exhibited a dark precipitated phase (Fig. 2(b)) and an equiaxed dark structure composed of fine grains encased within a bright phase, as evidenced in Fig. 2(b-1). EDS results suggest that these dark precipitated phases shown in Fig. 2(b) are $(Zr, Hf, Ti)_2Al$ phases. It was observed that Ti and Hf contents are slightly high in the bright phases in the matrix and Zr and Al contents are slightly high in the dark phase. The presence of the dark precipitated phase is consistent with our previous findings [16], suggesting that the alloy composition adjustment did not eliminate the presence of precipitates although the volume fraction of precipitates drastically decreased.

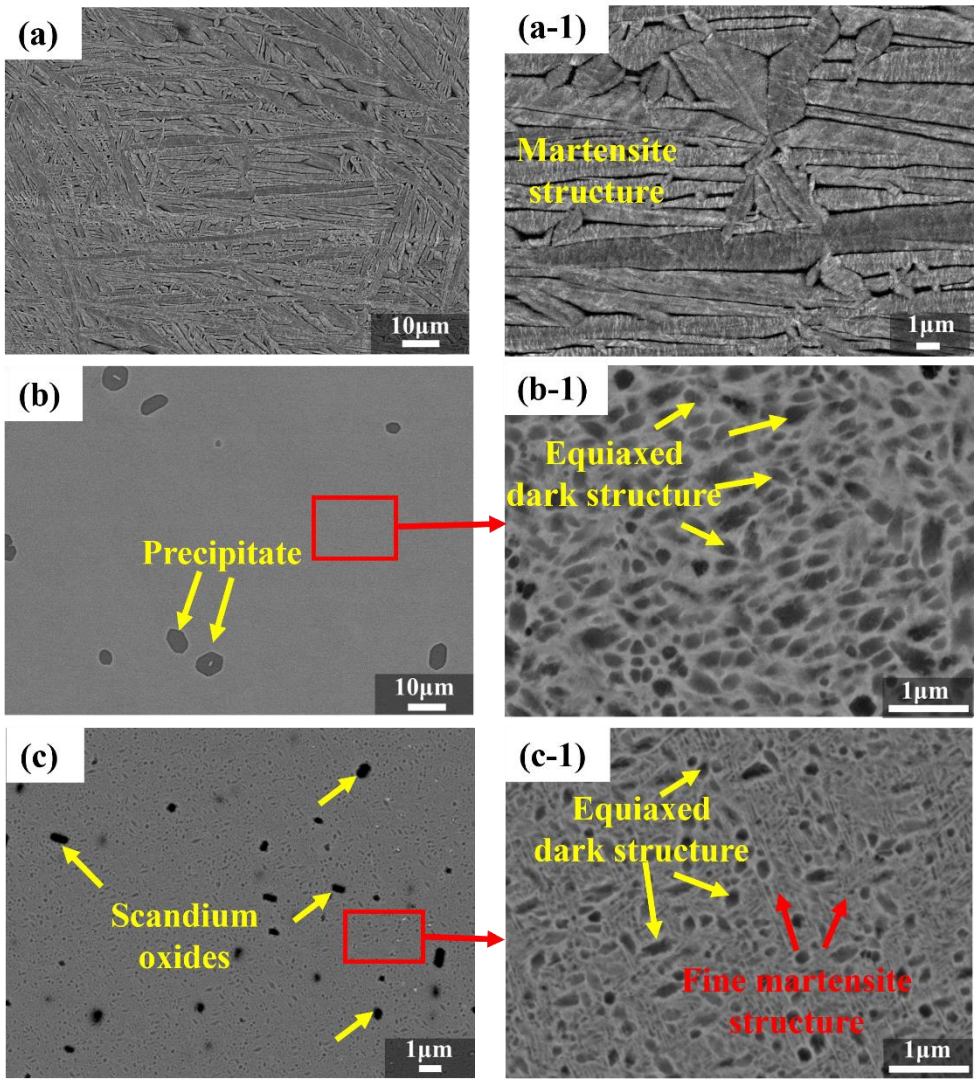


Fig. 2 Backscattered images of the specimens rolled at 1000℃: (a) TiZrHf, with high magnification (a-1), (b) TiZrHfAl, and high magnification of the matrix region marked by the red line (b-1), (c) TiZrHfAlSc and high magnification of the matrix region marked by the red line (c-1).

Table 3 Phase composition (at%) of as-rolled specimens investigated by EDS.

Alloy	Region	Ti	Zr	Hf	Al	Sc	O
TiZrHf	Martensite	32.7	33.1	34.2	-	-	-
TiZrHfAl	Dark Precipitated phases	16	26.3	23.8	33.9	-	-
	Dark phase	28.0	24.1	28.6	19.3	-	-
	Bright phase	32.2	21.0	29.0	17.8	-	-
TiZrHfAlSc	Black regions	12.2	11.0	11.0	11.3	29.5	25.0
	Fine equiaxed	20.1	20.4	18.0	20.2	21.3	-
	Fine martensite	21.9	20.1	18.8	19.0	20.2	-

X-ray diffraction analysis was conducted for the heat-treated samples. The heat treatment condition was 800 °C for 24 hours for TiZrHf and TiZrHfAlSc and 168 hours for TiZrHfAl followed by furnace cooling. The XRD patterns are shown in Fig. 3. Intense peaks of the hcp-phase (space group 194) are present in all three specimens, yet distinctions exist among them. The TiZrHf specimen displays a single peak corresponding to the hcp-phase with lattice constants of a = 3.15Å, c =5.03Å, and c/a=1.60. Notably, in the TiZrHfAl specimen, the lattice constants were a = 3.05Å, c =4.86Å, and c/a=1.59. We also identify peaks associated with hcp-Zr_2Al, despite their subdued intensity. In the TiZrHfAlSc specimen, the lattice constants were a = 3.11Å, c =4.93Å and c/a=1.59, alongside the principal hcp-phase peaks, we discern additional faint unknown peaks.

In the microstructure of heat-treated samples depicted in Fig. 4 (a), the TiZrHf alloy maintains its martensite structure like its as-rolled condition. It exhibits a notable growth to plate-like structures with a width of 2-8 μm. Additionally, the coarse grain boundary hcp-phase, with widths reaching up to 10 μm, is formed along the grain boundaries, as depicted in Fig. 4(a, a-1). According to the results obtained from the chemical analysis by EDS shown in Table 4, these plate-like hcp structures exhibit an elemental distribution equal to the composition of the alloy.

On the other hand, in the TiZrHfAl alloy, three distinct microstructures were observed: (region 1): a dark precipitated phase surrounded by bright phases, (region 2): a bright phase formed along grain boundaries and dark precipitated phase, and (region 3, 4): a

comparatively fine equiaxed structure in the matrix as shown in Fig. 4 (b, b-1). ImageJ analysis revealed that the dark precipitated phase has irregular shapes measuring 6 to 15 μm in length and 2 to 5 μm in width, constituting 6% of the total volume. Upon closer examination of the fine matrix phase, it is composed of both dark and bright phases, each with grain sizes around 1-3 μm and exhibiting an equiaxed morphology (Fig. 4 (b-1)). EDS elemental analysis, as shown in Table 4, indicates that the bright phases formed surrounding the dark precipitated phase (Region 2 in Fig. 5 (a)) are low in Al content, 14.5 at%, compared with another phase. In contrast, the dark precipitates (Region 1 in Fig. 5 (a)) show 33.2 at% of Al. The EBSD phase map distinctly demonstrates that the bright phases (Region 1) are hcp phases (Fig. 6 (b)). Conversely, the dark precipitated phase (Region 2) is identified as 194-Zr_2Al. In the fine phases of the matrix, the composition difference between the bright regions (Region 4 in Fig. 5 (b)) and the dark phases (Region 3 in Fig. 5 (b)) is minimal, but the Hf contents in the bright phase are 1 at% higher than in the dark phase. This small difference in the Hf contents caused the different contrast of the phases in Fig. 4 (b-1). Analysis of the XRD pattern in Fig. 3 and the EBSD phase map in Fig. 6 (c) indicate these phases are hcp phases.

In the TiZrHfAlSc alloy, we observed the formation of a fine plate-like structure from the fine martensite structure that had developed during the rolling process (Fig. 4 (c)), consistent with other finding [19]. Even though these plates became coarser than those observed in Fig. 2 (c-1), their thickness remained less than 1 μm. XRD pattern analysis suggests that the plate-like structure is the hcp-phase. However, unlike in the TiZrHfAl alloy, heat treatment eliminated the finer dark equiaxed phase within the matrix observed in the as-rolled specimens. In addition, elliptical black particles were still observed (Fig. 4 (c, c-1)), as indicated by red arrows. EDS analysis revealed a high concentration of Sc and O in these areas, suggesting the presence of Sc oxides introduced during the rolling process, even though no specific peaks for these oxides were detected in the XRD pattern. Oxides of Sc also appeared in other reports in TiZrHfSc [16] because the Sc was easily oxidized and even the addition of Al could not prevent the oxidation of Sc.

These results show that the TiZrHf alloy developed a coarsened martensite structure without any precipitates. In contrast, the TiZrHfAl alloy formed two hcp phases with slightly different compositions, along with Zr_2Al precipitates. Meanwhile, the TiZrHfAlSc alloy displayed a fine plate-like hcp phase, and Sc_2O_3 precipitates.

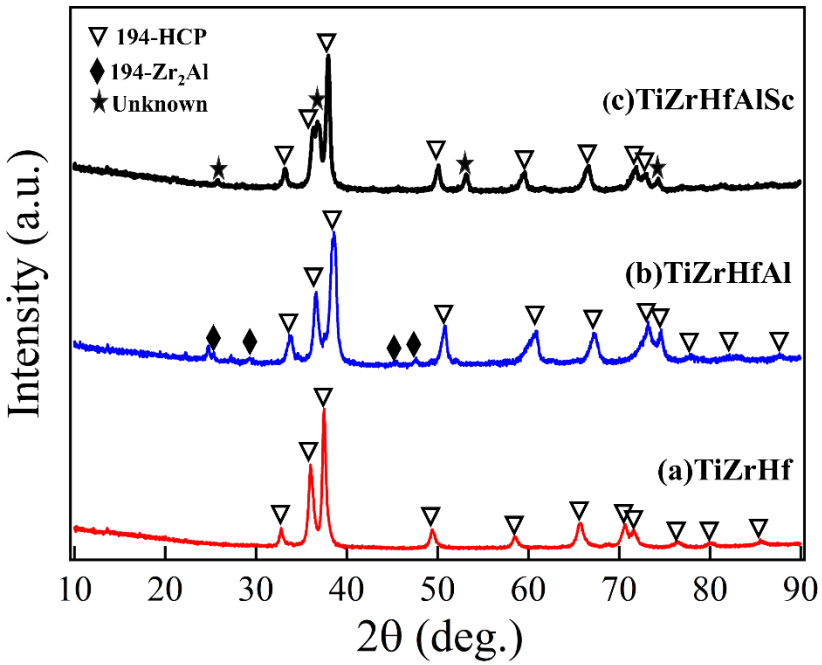


Fig. 3 XRD patterns of the specimens (a) TiZrHf, (b) TiZrHfAl, (c) TiZrHfAlSc, after heat-treatment at 800°C for 24h and 168h followed by furnace cooling.

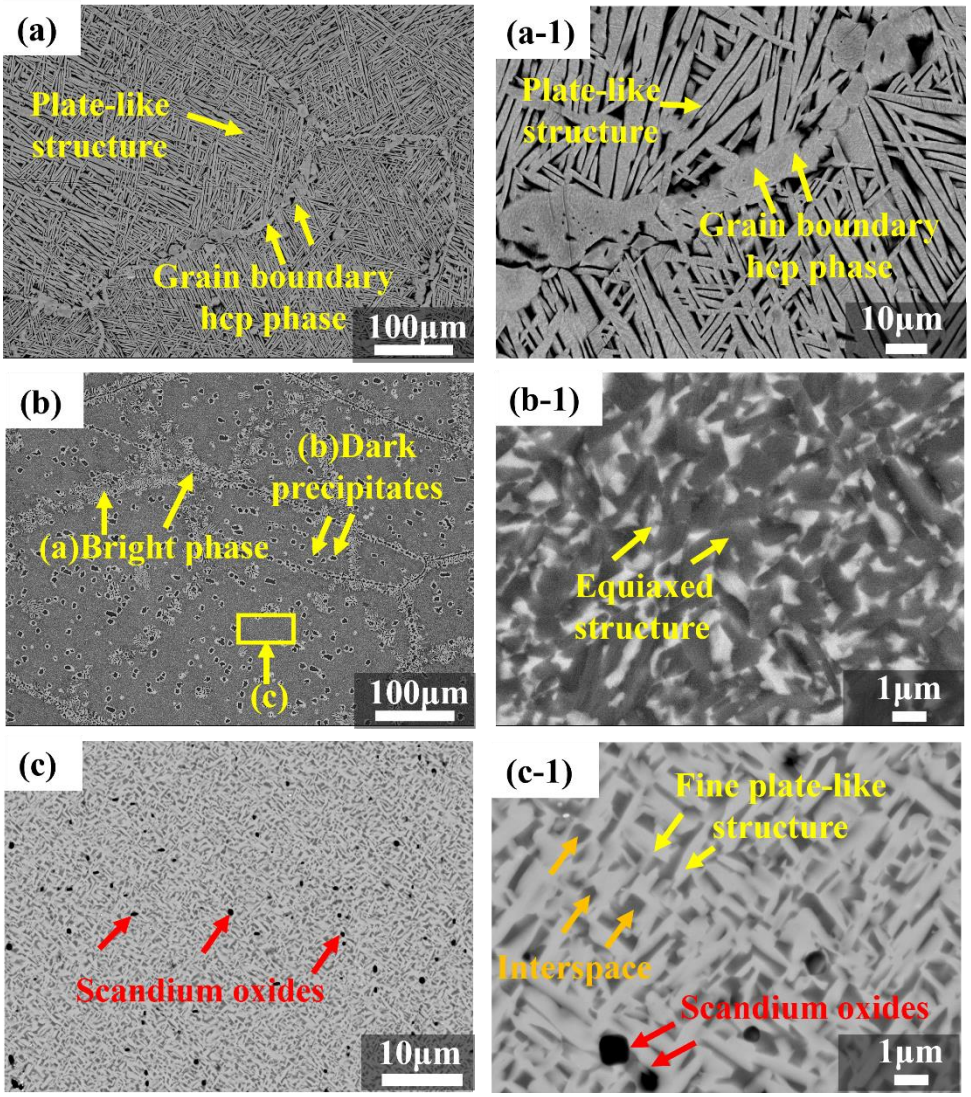


Fig. 4 Backscattered images of specimens heat-treated at 800℃ for 24h with furnace cooling: (a) TiZrHf, with a high-magnification view (a-1), (c) TiZrHfAlSc, and high magnification (c-1). Additionally, (b) TiZrHfAl and a high-magnification view (b-1) are presented for specimens heat-treated at 800℃ for 168h followed by furnace cooling.

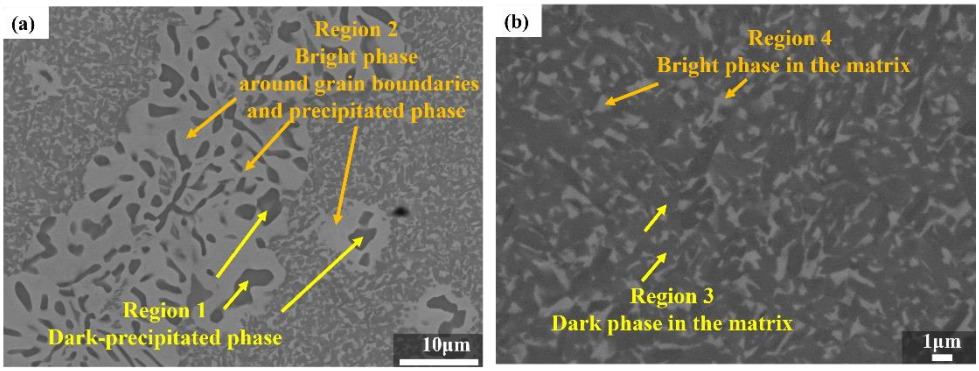


Fig. 5 Elemental analysis of designated regions in TiZrHfAl specimens after heat treatment through EDS.

Table 4 Phase composition (at%) of alloys after heat treatment investigated by EDS.

Heat-treatment condition	Alloy	Region	Ti	Zr	Hf	Al	Sc	O	Phase
800℃ 24h FC	TiZrHf	Plate-like phase	33.5	32.6	33.9	-	-	-	hcp
800℃ 168h FC	TiZrHfAl	1	19.5	25.5	22.8	32.2	-	-	Zr_2Al-194
		2	33.8	20.0	31.7	14.5	-	-	hcp
		3	31.3	21.7	26.9	20.1	-	-	hcp
		4	31.4	21.5	28.1	19	-	-	hcp
800℃ 24h FC	TiZrHfAlSc	Dark	12.3	9.3	8.7	10.2	25.5	34	Sc_2O_3
		Plate-like phase	20.2	19.6	18.9	16.3	16.4	8.6	hcp

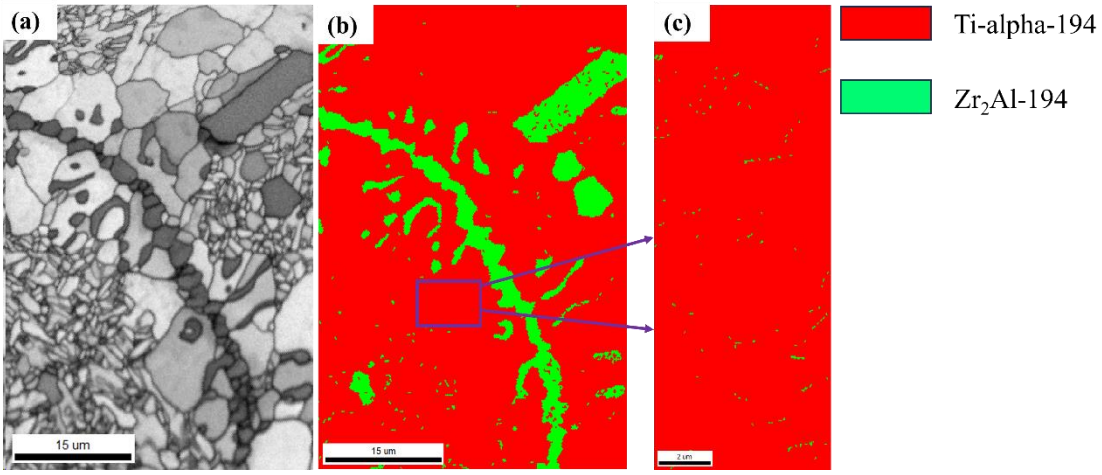


Fig. 6 Electron Back Scatter Diffraction (EBSD) images of TiZrHfAl heat-treated at 800℃ for 168h with furnace cooling: (a) Image Quality (IQ) map focusing on the grain boundary and precipitates, (b) Phase map of grain boundary and precipitates, (c) Phase map of fine matrix region.

3.2 Mechanical properties

Compression tests were performed on TiZrHf and TiZrHfAlSc alloy specimens, which were heat-treated at 800°C for 24 hours followed by furnace cooling, and on TiZrHfAl alloy specimens treated under the same temperature for 168 hours followed by furnace cooling, to evaluate their high-temperature strength. As shown in Fig. 4, the TiZrHf alloy exhibited a coarsened plate-like structure, the TiZrHfAlSc alloy revealed a finer plate-like structure interspersed with ScO_2. In contrast, the TiZrHfAl was characterized by an equiaxed hcp phase with a Zr_2Al precipitated phase.

Fig. 7 illustrate the 0.2% proof stress at 400 and 600 °C for the studied alloys. The mixing entropy, ΔS_{mix}, and δ parameters are also shown in Fig. 7. The TiZrHfAlSc alloy exhibited highest strength in the 400 and 600 °C, but it fractured during the elastic deformation stage at 400 °C, which can be postulated that the 0.2% proof stress for this alloy should be higher than what is indicated in Fig. 7. The 0.2% proof stress of TiZrHfAl alloy was the secondary highest at 400 and 600 °C. The 0.2% proof stress of the TiZrHf alloy was the lowest at 400 and 600 °C. Although the microstructures of these alloys are different, the higher strength was shown in the alloy with larger ΔS_{mix} and δ parameters. The 0.2% proof stress of the TiZrHfAlSc and TiZrHfAl were over 900 MPa at 600 ˚C, higher than those of commercial Ti alloys such as TIMETAL 834 about 500 MPa [25].

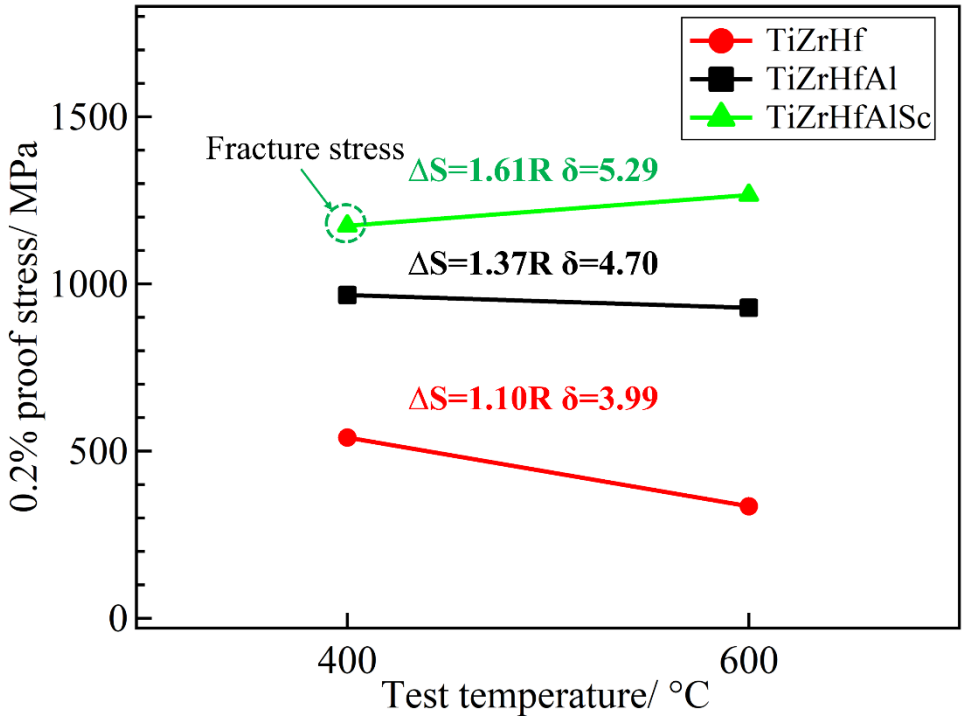


Fig. 7 0.2% proof stress of TiZrHf, TiZrHfAl, TiZrHfAlSc specimens by compression test at 400℃ and 600℃.

3.3 Deformation behavior

To investigate the deformation mechanism of the equiaxed hcp structure, a compression strain rate jump test was performed on the TiZrHfAl specimen heat-treated at 800℃ for 168h followed by furnace cooling. The compressive stress-strain curves obtained from the strain rate jump test at room temperature and 600℃ are shown in Figs. 8 (a) and (b), respectively. In the strain rate jump test, strain rate change causes a sharp increase in stress [26]. As shown in Fig. 8, the stress jump was observed at each strain rate change, except for the first strain rate change at room temperature, which was too small to be observed. Based on these stress changes, the 0.2% proof stress corresponding to each different strain rate at room temperature and 600℃ was measured and summarized in Table 5.

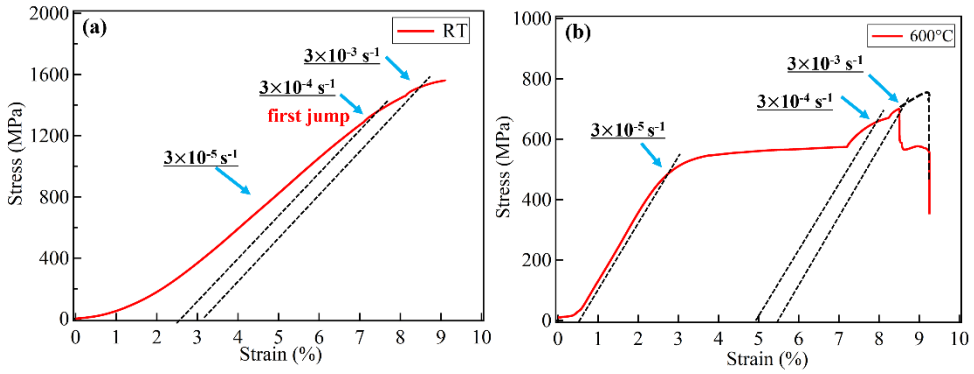


Fig. 8 Stress and strain curves at (a) room temperature and (b) 600℃, by stain rate jump test for TiZrHfAl alloy.

Table 5 The 0.2% proof stress corresponds to each different strain rate at room temperature and 600℃.

Temperature (℃)	**0.2% proof stress (MPa)**		
	3×10^{-5} s^{-1}	**3×10^{-4} s^{-1}**	**3×10^{-3} s^{-1}**
RT	1393	1395	1528
600	502	655	725

Like the investigation approach used to study the high-temperature deformation mechanism of conventional titanium alloys, an Arrhenius-type equation was used to express the strain rate $\dot{\varepsilon}$ [27].

$$\dot{\varepsilon} = A\sigma^{n} exp\left(-\frac{Q}{RT}\right) \tag{3}$$

where A is the material constant, σ is the stress, n is the stress exponent, Q is the activation energy for deformation, R is a gas constant, and T is the temperature.Taking the natural logarithm of both sides gives:

$$\ln\dot{\varepsilon} = \ln(A) + n\ln\sigma - \frac{Q}{R}\left(\frac{1}{T}\right) \tag{4}$$

The stress exponent n can be calculated from the slope using a double logarithm plot of $\ln\dot{\varepsilon}$ and $\ln\sigma$ in equation (4). The 0.2% proof stress was used as σ to estimate the stress exponent n.

The double logarithm plot of the strain rate $\dot{\varepsilon}$ and 0.2% proof stress σ at room temperature and 600℃ are shown, as shown in Fig. 9. The stress exponent value was approximately

18 at room temperature and 5 at 600°C. It exhibited a large stress exponent at room temperature, and the stress exponent at 600 °C was essentially the same as that of conventional heat-resistant titanium alloys [28].

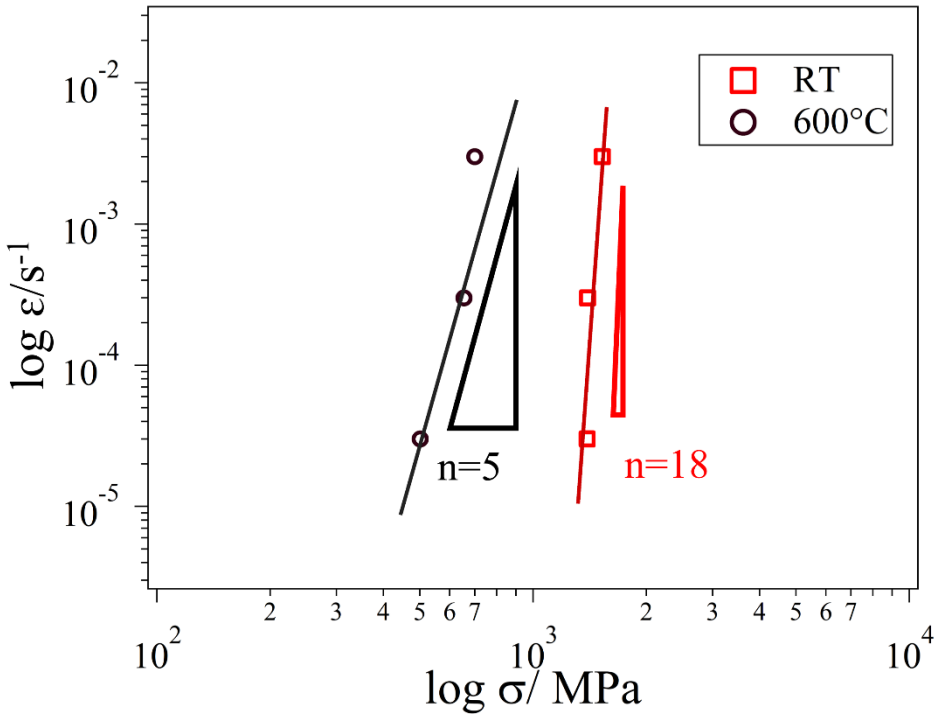


Fig. 9 Double logarithm plot of the stress and strain rate of TiZrHfAl sample obtained by strain rate jump test at RT and at 600°C.

High-temperature deformation is a thermally activated process, and the thermally activated mechanisms of compressive deformation can be quantitatively expressed using the activation volume, V^*, defined as the volume that dislocation can move by overcoming obstacles during deformation [29][30]. The activation volume which is normally expressed in a unit of b^3 (b is the Burgers vector), V^*, is defined as the following equation (5).

$$V^* = \sqrt{3}kT(\partial ln\dot{\varepsilon}/\partial\sigma) \quad (5)$$

where k is the Boltzmann's constant, and the T is the absolute temperature. The activation volumes were calculated and summarized in Table 6. As shown in Table 6 the activation volume of TiZrHfAl increased with increasing temperature and strain rate, reaching values of 15-35 b^3 at 600°C. The activation volumes of pure Ti and Mg with hcp structures and those of recently reported bcc high-entropy alloy TiZrHfNb were also summarized for comparison in Table 6. It can be found that the activation volume of TiZrHfAl is 6.3

at room temperature, which is approximately the same order as 4 for TiZrHfNb of the bcc-type high-entropy alloy in another study [31]. The activation volumes of TiZrHfAl at 600 ℃ were within the same range as those of Ti, Mg, and their alloys at room temperature [32–34].

Table 6 The activation volume measured from the strain rate jump tests at RT and 600℃ of the TiZrHfAl sample.

Temperature (℃)	**3×10^{-5} ~3×10^{-4} s^{-1}**	**3×10^{-4} ~3×10^{-3} s^{-1}**	**Pure Ti** [32]	**Ti-6Al-4V** [33] **Pure Mg** [34]	**BCC-HEA TiZrHfNb** [31]
	V^* (b^3)		***V^* (b^3)***		
RT	-	6.3	35	25	4.3
600	15.8	34.8	-	-	-

4. Discussion

4.1 Microstructure formation

In addition to TiZrHfAl, previous investigations have confirmed the presence of hcp phases in TiZrHf and TiZrHfAlSc alloys[14–16,19]. However, the investigations were performed for as-cast[14,15] or just heat-treated for homogenization[16][19], and then the observed microstructures in these alloys have primarily exhibited martensite and plate-like structures. To achieve the equiaxed hcp structure, distinct from the prevailing martensite microstructure, the appropriate manufacturing process is important. It is well known that in the traditional titanium alloy, thermomechanical and subsequent heat treatment in the α+β two-phase region can produce the equiaxed structure by recrystallization assisted by dense dislocation density introduced during deformation. [35].

In this study, thermomechanical processing followed by heat treatment was conducted on TiZrHf, TiZrHfAl, and TiZrHfAlSc alloys. As depicted in Fig. 4(b, b-1), the successful formation of equiaxed hcp phases in the TiZrHfAl alloy was achieved. In the TiZrHfAl alloy, the thermomechanical processing was conducted at 1000 ℃ in the hcp phase region. The initial microstructure was broken during deformation and dynamic recrystallization of the hcp phase occurred during subsequent reheating at 1000℃, as illustrated in Fig. 2 (b-1). Following heat treatment at 800 ℃ in the hcp phase region, these recrystallized equiaxed grains grew and became more uniform. Although the phase diagram indicates a single hcp phase, two hcp phases with small composition differences were formed. This

might occur in compositional fluctuation in HEAs. At 800℃, the phase diagram in Fig. 1 (e) suggests the formation of Al_2Zr_3 phases. However, Zr_2Al phases were observed in our experiment. This discrepancy indicates that the phase equilibria predicted by Thermo Calc differed from the experimental results.

Conversely, the equiaxed structure was not formed in TiZrHf and TiZrHfAlSc. The thermomechanical treatment temperature of 1000℃ is the bcc phase in TiZrHf, as shown in Fig. 1(d). The martensite structure in the processed sample (Fig. 2 (a-1)) indicates that the dislocations induced during rolling were released during reheating after rolling, and then thermomechanical treatment did not affect breaking the martensite structure. The subsequent heat treatment at 800℃ in the hcp phase just coarsen the martensite structure. A similar microstructure was obtained in TiZrHfAlSc, although the structure was finer than in TiZrHf. The phase diagram of TiZrHfAlSc was not clear, but it is expected that the bcc phase was stable at 1000 ℃ in TiZrHfAlSc. This also indicates that TiZrHf, thermomechanical treatment was insufficient to introduce dislocations for accelerating nucleation of the hcp phase during subsequent heat treatment.

4.2 Mechanical properties

As shown in Fig. 7, the 0.2 % proof stress increased with the increase of the mixing entropy, ΔS_{mix} and the average atomic size misfit, δ. It is well known that solid-solution strengthening in binary alloys with higher concentrations of solute atoms (x_i) is shown in equation (6) [36].

$$\Delta\sigma_{ss} = B_i x_i^{2/3} \tag{6}$$

where the parameters B_i is

$$B_i = 3\mu\varepsilon_i^{4/3} Z \tag{7}$$

where μ is the shear modulus of the alloy and Z is a fitting constant.

The parameters ε_i is the sum of the elastic misfit η_i' and the atomic size misfit δ_i between two dissimilar atoms.

$$\varepsilon_i = (\xi\eta_i'^2 + \alpha^2\delta_i^2)^{1/2} \tag{8}$$

where ξ is related to the activated slip systems, and α is the lattice parameter of the alloy. From equation (6) ~ (8), the solid solution strengthening is proportional to 3/4 ths of the atomic size misfit.

This equation was expanded to HEAs and expressed as the following equation (9) by Gypen [37] and Toda-Caraballo [38,39].

$$\sigma_{ss} = \left(\sum_i B_i^{3/2} x_i\right)^{2/3};\ B_i = M\mu{\varepsilon_i}^{4/3} Z \tag{9}$$

The solid solution strengthening is expressed by the sum of the effect of elastic misfit and

the atomic size misfit for all combinations of the constituent elements. From equations (8) and (9), the increase of the atomic size misfit δ_i increases the solid solution strengthening. The average atomic size misfit δ in equation (2) is the average of all combinations of the constituent elements and is different from the atomic size misfit δ_i where two dissimilar atoms are compared. However, if the sum of the atomic size misfit δ_i increases, the average atomic size misfit δ also increases. Then, an increase in the average atomic size misfit δ causes an increase in the solid solution strengthening effect. In our study, three alloys represented different microstructures, but they were consisted of the hcp phase. The increase in the average atomic size misfit δ indicates an increase in solid solution strengthening of the hcp phase. Then, it is reasonable that the strength of the alloy with a higher δ was higher.

To our knowledge, there is no explanation of the solid-solution strengthening effect directly related to the mixing entropy ΔS_{mix}. However, an increase in the mixing entropy indicates a high probability that atoms of different species will be next to each other. This causes lattice distortion and increases the solid-solution strength together with the atomic size misfit. Our experimental results support the effect of the mixing entropy on the solid solution strengthening.

Table 7 Comparative analysis of 0.2% proof stress in TiZrHf, TiZrHfAl, TiZrHfAlSc alloys under compression at 400℃ and 600℃ concerning other studies.

Alloy composition	Process	Microstructure	Thick-ness (μm)	Test temperature (℃)	σ_y (MPa)	Ref.
TiZrHf	Rolled and heat-treated	Plate-like	2-5	400 600	541 335	This study
	As-cast	Plate-like	-	RT	773	[14]
	As-cast	plate-like	2-5	RT	901	[15]
	As-cast + heat-treated	Martensite	-	RT 600	900 300	[16]
TiZrHfAl	Rolled and heat-treated	Equiaxed-hcp with Zr_2Al	1	400 600	967 928	This study
	As-cast + heat-treated	Bcc with Zr_2Al	-	600	1000	[16]
TiZrHfSc	As-cast	Plate-like-hcp	1-2	RT	1001	[14]
	As-cast + heat-treated	Plate-like-hcp	1-3	RT	800	[16]
	As-cast	Plate-like-hcp	2-3.5	RT	698	[17]
TiZrHfAlSc	Rolled and heat-treated	Plate-like-hcp	0.1-0.5	400 600	1174 1265	This study
	As-cast	Plate-like -hcp	0.3-0.8	RT	1450	[19]

Table 7 summarizes the microstructures and strengths investigated in the previous studies to compare our results. The strength of the TiZrHf with the plate-like structure was 900 MPa [15] at room temperature and 335 MPa at 600 ℃ in our study. The strength of the TiZrHf with the martensite structure was 900 and 300 MPa at room temperature and 600 ℃, respectively [16]. These results indicate that the strengths of TiZrHf were similar values independent of microstructure, either the plate-like or martensite structures. In addition, the TiZrHf alloys do not exhibit exceptional high-temperature strength compared to conventional alloys, with a strength of approximately 500 MPa at 590 ℃ for TIMETAL 834 [25].

For hcp-TiZrHfAl alloy, no strength data was found even at both room temperature

and high temperature. The strength of bcc-TiZrHfAl [16] was compared with that of hcp-TiZrHfAl. Their strengths were almost the same, even with the difference in crystal structure and the volume fraction of Zr_2Al.

For TiZrHfAlSc alloy with a plate-like structure, only room temperature strength was reported in [19]. The high strength at room temperature indicates the significant effect of the atomic size misfit as well as our high-temperature results.

In Table 7, the strength of TiZrHfSc [16] at room temperature is also shown. The strength varied between 700 and 1000 MPa, which may be due to the difference in the thickness of the martensite plate. The finer structures correlate to higher strength levels. Compared with the strength of TiZrHfAl and TiZrHfSc, the strength of TiZrHfAl at 400 and 600 °C were similar value with the strength of TiZrHfSc at room temperature. The average atomic size misfit (δ) is 3.99 for TiZrHf, 4.26 for TiZrHfSc, and 4.79 for TiZrHfAl. This suggests that Al more effectively enhances the average atomic size misfit (δ), significantly boosting strength compared to Sc.

4.3 Deformation mechanisms

Fig. 9 illustrates that the TiZrHfAl alloy possesses an exceptionally high stress exponent of 18 at room temperature, substantially surpassing those in the range of 3 and 5 in many traditional Ti alloys [40–42]. Typically, a stress exponent above 8 indicates precipitation strengthening [40,43,44]. The 6% volume fraction of Zr_2Al was observed as shown in Fig. 4(b), but the effect will be small due to the low volume fraction. It is suggested that atomic-level chemical fluctuation occurs in high-entropy alloys [45]. This disarray can result in short-range order where dissimilar atoms gather or clusters where similar atoms gather at the atomic level. These compositional fluctuations potentially hinder dislocation movement. Table 5 reveals that the activation volume for dislocation motion in TiZrHfAl at room temperature is notably smaller, at 6.3 b^3, much lower than the standard hcp metals and alloys, which typically exhibited 25-35 b^3 [32–34]. Similar trends of low activation volumes are observed in other TiZrHf series high-entropy alloys, such as the bcc-TiZrHfNb alloy with an activation volume of 4.3 b^3 [31]. Wu et al. [46] introduce an improved Laubsch model, suggesting that high-entropy alloys with smaller activation volumes have a more pronounced contribution from short-range order effects. Consequently, it is postulated that the elevated stress exponent in the TiZrHfAl alloy could be attributed to dislocations navigating through small obstacles like atomic clusters in a short-range order, leading to a higher stress exponent and a reduced activation volume.

At 600°C, the TiZrHfAl alloy exhibits a stress exponent of 4.8, suggesting dislocation slip as the predominant deformation mechanism, like that in traditional solid-solution-

strengthened alloys [41,42]. Notably, there is an increase in activation volume at 600°C compared to room temperature, aligning with the activation volumes found in typical hcp-type Ti and Mg metals at room temperature. This indicates that the small obstacles, like the cluster of irregular atoms effective at room temperature, offer less resistance at 600°C. Cross slip, frequently observed in standard hcp alloys such as hcp-Ti and Mg, which show similar activation volumes to the TiZrHfAl alloy at 600 ℃, may also be a plausible mechanism in this alloy. Furthermore, reports indicate that titanium alloys display lower critical resolved shear stress (CRSS) values for both basal {0001} and prismatic $\{10\bar{1}0\}$ slip planes at 600 °C [47]. This finding corroborates the tendency of hcp-type alloys to exhibit more cross-slip at elevated temperatures.

5 Conclusions

This study applied a thermomechanical process, including hot rolling and heat treatment, to develop equiaxed hcp phases in TiZrHf, TiZrHfAl, and TiZrHfAlSc alloys. High-temperature mechanical properties were assessed using compression tests, with a focus on the deformation mechanisms in the TiZrHfAl alloy. Key findings include:

1) Hot rolling at 1000 °C and heat treatment at 800 °C resulted in the formation of equiaxed dual hcp structures about 1 μm in size in TiZrHfAl alloys, while TiZrHf and TiZrHfAlSc alloys primarily formed plate-like hcp structures.
2) The 0.2% proof stress of the alloys showed a consistent increase with the increase in the mixing entropy ΔS_{mix} and average atomic size misfit δ. Both TiZrHfAl and TiZrHfAlSc alloys exhibited compressive strength exceeding 900 MPa at 600 ℃, significantly surpassing conventional heat-resistant titanium alloys.
3) The TiZrHfAl exhibits a high stress exponent of 18 and low activation volume at room temperature, suggesting a mechanism of strengthening with interruption of dislocation movement from minor obstacles such as atomic clusters or short-range orders in HEAs. At 600 ℃, a lower stress exponent and larger activation volume indicate that deformation is primarily due to dislocation slip, facilitated by cross slip.

Acknowledgments

This work was supported by Grants-in Aid for Transformative Research Area A, 21H05198 and The Light Metal Educational Foundation (Japan). We appreciate to Mr. K. Iida, M. S. Iwasaki, Mr. M. Kobayashi in NIMS for rolling ingots.

Declaration of generative AI in scientific writing

During the preparation of this work, the authors used Grammary and ChatGPT in order to improve the readability and language of this work. After using this tool, the authors reviewed and edited the content as needed and took full responsibility for the content of the publication.

Data Availablity

The raw/processed data required to reproduce these findings cannot be shared at this time as the data also forms part of an ongoing study.

Reference

[1] C. (Christoph) Leyens, M. (Manfred) Peters, Titanium and titanium alloys : fundamentals and applications, Wiley-VCH, 2003.

[2] M. Peters, J. Kumpfert, C.H. Ward, C. Leyens, Titanium Alloys for Aerospace Applications, Adv Eng Mater 5 (2003) 419–427. https://doi.org/10.1002/adem.200310095.

[3] K. SUZUKI, K. NAKAMURA, S. KATO, A. YAMAGISHI, Experimental Approach to Obtain a Comprehensive Understanding of the Biogeochemistry of a Seafloor Hydrothermal System, Chigaku Zasshi (Jounal of Geography) 118 (2009) 1131–1159. https://doi.org/10.5026/jgeography.118.1131.

[4] J.-W. Yeh, S.-K. Chen, S.-J. Lin, J.-Y. Gan, T.-S. Chin, T.-T. Shun, C.-H. Tsau, S.-Y. Chang, Nanostructured High-Entropy Alloys with Multiple Principal Elements: Novel Alloy Design Concepts and Outcomes, Adv Eng Mater 6 (2004) 299–303. https://doi.org/10.1002/adem.200300567.

[5] E.P. George, D. Raabe, R.O. Ritchie, High-entropy alloys, Nat Rev Mater 4 (2019) 515–534. https://doi.org/10.1038/s41578-019-0121-4.

[6] R.-X. Li, J.-W. Qiao, P.K. Liaw, Y. Zhang, Preternatural Hexagonal High-Entropy Alloys: A Review, Acta Metallurgica Sinica (English Letters) 33 (2020) 1033–1045. https://doi.org/10.1007/s40195-020-01045-9.

[7] J. Liu, X. Guo, Q. Lin, Z. He, X. An, L. Li, P.K. Liaw, X. Liao, L. Yu, J. Lin, L. Xie, J. Ren, Y. Zhang, Excellent ductility and serration feature of metastable CoCrFeNi high-entropy alloy at extremely low temperatures, Sci China Mater 62 (2019) 853–863. https://doi.org/10.1007/s40843-018-9373-y.

[8] Z. Zhang, M.M. Mao, J. Wang, B. Gludovatz, Z. Zhang, S.X. Mao, E.P. George, Q. Yu, R.O. Ritchie, Nanoscale origins of the damage tolerance of the high-entropy alloy CrMnFeCoNi, Nat Commun 6 (2015) 10143. https://doi.org/10.1038/ncomms10143.

[9] D. Li, C. Li, T. Feng, Y. Zhang, G. Sha, J.J. Lewandowski, P.K. Liaw, Y. Zhang, High-entropy Al0.3CoCrFeNi alloy fibers with high tensile strength and ductility at ambient and

cryogenic temperatures, Acta Mater 123 (2017) 285–294. https://doi.org/10.1016/j.actamat.2016.10.038.

[10] O.N. Senkov, G.B. Wilks, J.M. Scott, D.B. Miracle, Mechanical properties of Nb25Mo25Ta25W25 and V20Nb20Mo20Ta20W20 refractory high entropy alloys, Intermetallics (Barking) 19 (2011) 698–706. https://doi.org/10.1016/j.intermet.2011.01.004.

[11] W. Zhang, P. Liaw, Y. Zhang, A Novel Low-Activation VCrFeTaxWx (x = 0.1, 0.2, 0.3, 0.4, and 1) High-Entropy Alloys with Excellent Heat-Softening Resistance, Entropy 20 (2018) 951. https://doi.org/10.3390/e20120951.

[12] O.N. Senkov, J.M. Scott, S.V. Senkova, D.B. Miracle, C.F. Woodward, Microstructure and room temperature properties of a high-entropy TaNbHfZrTi alloy, J Alloys Compd 509 (2011) 6043–6048. https://doi.org/10.1016/j.jallcom.2011.02.171.

[13] A. Takeuchi, K. Amiya, T. Wada, K. Yubuta, W. Zhang, High-Entropy Alloys with a Hexagonal Close-Packed Structure Designed by Equi-Atomic Alloy Strategy and Binary Phase Diagrams, JOM 66 (2014) 1984–1992. https://doi.org/10.1007/s11837-014-1085-x.

[14] T. Huang, H. Jiang, Y. Lu, T. Wang, T. Li, Effect of Sc and Y addition on the microstructure and properties of HCP-structured high-entropy alloys, Applied Physics A 125 (2019) 180. https://doi.org/10.1007/s00339-019-2484-1.

[15] S. Wang, D. Wu, H. She, M. Wu, D. Shu, A. Dong, H. Lai, B. Sun, Design of high-ductile medium entropy alloys for dental implants, Materials Science and Engineering: C 113 (2020) 110959. https://doi.org/10.1016/j.msec.2020.110959.

[16] Y. Yamabe-Mitarai, K. Yanao, Y. Toda, I. Ohnuma, T. Matsunaga, Phase stability of Ti-containing high-entropy alloys with a bcc or hcp structure, J Alloys Compd 911 (2022) 164849. https://doi.org/10.1016/j.jallcom.2022.164849.

[17] Ł. Rogal, F. Czerwinski, P.T. Jochym, L. Litynska-Dobrzynska, Microstructure and mechanical properties of the novel Hf25Sc25Ti25Zr25 equiatomic alloy with hexagonal solid solutions, Mater Des 92 (2016) 8–17. https://doi.org/10.1016/j.matdes.2015.11.104.

[18] S. Uporov, S.Kh. Estemirova, V.A. Bykov, D.A. Zamyatin, R.E. Ryltsev, A single-phase ScTiZrHf high-entropy alloy with thermally stable hexagonal close-packed structure, Intermetallics (Barking) 122 (2020) 106802. https://doi.org/10.1016/j.intermet.2020.106802.

[19] L. Rogal, P. Bobrowski, F. Körmann, S. Divinski, F. Stein, B. Grabowski, Computationally-driven engineering of sublattice ordering in a hexagonal AlHfScTiZr high entropy alloy, Sci Rep 7 (2017) 2209. https://doi.org/10.1038/s41598-017-02385-w.

[20] T. Nagase, M. Todai, T. Nakano, Development of Ti–Zr–Hf–Y–La high-entropy alloys with dual hexagonal-close-packed structure, Scr Mater 186 (2020) 242–246. https://doi.org/10.1016/j.scriptamat.2020.05.033.

[21] A. Takeuchi, K. Amiya, T. Wada, K. Yubuta, Dual HCP structures formed in senary

ScYLaTiZrHf multi-principal-element alloy, Intermetallics (Barking) 69 (2016) 103–109. https://doi.org/10.1016/j.intermet.2015.10.022.

[22] L. Rogal, Y. Ikeda, M. Lai, F. Körmann, A. Kalinowska, B. Grabowski, Design of a dual-phase hcp-bcc high entropy alloy strengthened by ω nanoprecipitates in the Sc-Ti-Zr-Hf-Re system, Mater Des 192 (2020) 108716. https://doi.org/10.1016/j.matdes.2020.108716.

[23] T. Nagase, M. Todai, P. Wang, S.-H. Sun, T. Nakano, Design and development of (Ti, Zr, Hf)-Al based medium entropy alloys and high entropy alloys, Mater Chem Phys 276 (2022) 125409. https://doi.org/10.1016/j.matchemphys.2021.125409.

[24] G.-Y. Gan, L. Ma, D.-M. Luo, S. Jiang, B.-Y. Tang, Influence of Al substitution for Sc on thermodynamic properties of HCP high entropy alloy Hf0.25Ti0.25Zr0.25Sc0.25-xAlx from first-principles investigation, Physica B Condens Matter 593 (2020) 412272. https://doi.org/10.1016/j.physb.2020.412272.

[25] D.F. Neal, Development of TIMETAL 834, Materials Design Approaches and Experiences as Held during the TMS Fall Meeting (2001) 199–213.

[26] S. Venkadesan, P. Rodriguez, K.A. Padmanabhan, P.V. Sivaprasad, C. Phaniraj, Flow transients during strain rate jump tests in a titanium-modified austenitic stainless steel, Materials Science and Engineering: A 154 (1992) 69–74. https://doi.org/10.1016/0921-5093(92)90364-7.

[27] Z. Tobolová, J. Čadek, An interpretation of steady state creep, Philosophical Magazine 26 (1972) 1419–1428. https://doi.org/10.1080/14786437208220352.

[28] K. Shimagami, T. Ito, Y. Toda, A. Yumoto, Y. Yamabe-Mitarai, Effects of Zr and Si addition on high-temperature mechanical properties and microstructure in Ti-10Al-2Nb-based alloys, Materials Science and Engineering A 756 (2019) 46–53. https://doi.org/10.1016/j.msea.2019.04.031.

[29] J.L.M. D. Caillard, Thermally activated mechanisms in crystal plasticity, Elsevier, Amsterdam, 2003.

[30] R.J. Asaro, S. Suresh, Mechanistic models for the activation volume and rate sensitivity in metals with nanocrystalline grains and nano-scale twins, Acta Mater 53 (2005) 3369–3382. https://doi.org/10.1016/j.actamat.2005.03.047.

[31] Y.X. Ye, Z.P. Lu, T.G. Nieh, Dislocation nucleation during nanoindentation in a body-centered cubic TiZrHfNb high-entropy alloy, Scr Mater 130 (2017) 64–68. https://doi.org/10.1016/j.scriptamat.2016.11.019.

[32] G. Sargent, H. Conrad, STRESS RELAXATION AND THERNIALLY ACTIVATED DEFORMATION IN TITANIUM, Pergamon Press, Inc, 1969.

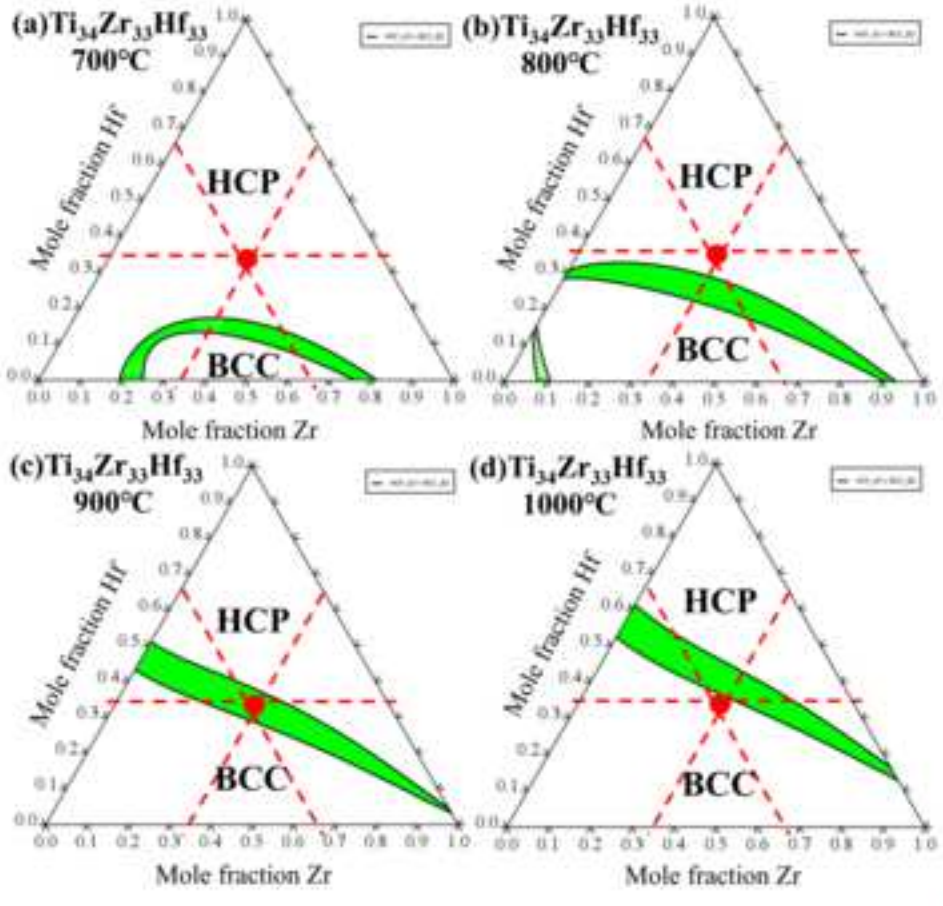
[33] B.R. Anne, M. Tanaka, T. Morikawa, Temperature Dependence of Activation Enthalpy for Yielding in Bimodal Ti–6Al–4V, Mater Trans 60 (2019) 1828–1832.

https://doi.org/10.2320/matertrans.ME201902.
[34] H. Somekawa, C.A. Schuh, Effect of solid solution elements on nanoindentation hardness, rate dependence, and incipient plasticity in fine grained magnesium alloys, Acta Mater 59 (2011) 7554–7563. https://doi.org/10.1016/j.actamat.2011.08.047.
[35] H. Masuyama, K. Shimagami, Y. Toda, T. Matsunaga, T. Ito, M. Shimojo, Y. Yamabe-Mitarai, Microstructure Evolution and Creep Behavior of Near-α Ti Alloy Produced by Thermomechanical Processing, Mater Trans 60 (2019) 2336–2345. https://doi.org/10.2320/matertrans.MT-MAW2019010.
[36] R. Labusch, A Statistical Theory of Solid Solution Hardening, Physica Status Solidi (b) 41 (1970) 659–669. https://doi.org/10.1002/pssb.19700410221.
[37] L.A. Gypen, A. Deruyttere, Multi-component solid solution hardening, J Mater Sci 12 (1977) 1028–1033. https://doi.org/10.1007/BF00540987.
[38] I. Toda-Caraballo, P.E.J. Rivera-Díaz-del-Castillo, Modelling solid solution hardening in high entropy alloys, Acta Mater 85 (2015) 14–23. https://doi.org/10.1016/j.actamat.2014.11.014.
[39] I. Toda-Caraballo, A general formulation for solid solution hardening effect in multicomponent alloys, Scr Mater 127 (2017) 113–117. https://doi.org/10.1016/j.scriptamat.2016.09.009.
[40] H. Hofmann, G. Frommeyer, C. Derder, Creep mechanisms in particle strengthened α-Titanium–Ti2Co alloys, Materials Science and Engineering: A 245 (1998) 127–134. https://doi.org/10.1016/S0921-5093(97)00714-4.
[41] H. MISHRA, D. SATYANARAYANA, T. NANDY, P. SAGAR, Effect of trace impurities on the creep behavior of a near α titanium alloy, Scr Mater 59 (2008) 591–594. https://doi.org/10.1016/j.scriptamat.2008.05.009.
[42] Z.Y. Ma, R.S. Mishra, S.C. Tjong, High-temperature creep behavior of TiC particulate reinforced Ti–6Al–4V alloy composite, Acta Mater 50 (2002) 4293–4302. https://doi.org/10.1016/S1359-6454(02)00261-6.
[43] J.C. Gibeling, W.D. Nix, The description of elevated temperature deformation in terms of threshold stresses and back stresses: A review, Materials Science and Engineering 45 (1980) 123–135. https://doi.org/10.1016/0025-5416(80)90218-9.
[44] K. Shimagami, S. Matsunaga, A. Yumoto, T. Ito, Y. Yamabe-Mitarai, Solid Solution Hardening and Precipitation Hardening of α2-Ti3;Al in Ti-Al-Nb Alloys, Mater Trans 58 (2017) 1404–1410. https://doi.org/10.2320/matertrans.MAW201707.
[45] S. Yoshida, T. Ikeuchi, T. Bhattacharjee, Y. Bai, A. Shibata, N. Tsuji, Effect of elemental combination on friction stress and Hall-Petch relationship in face-centered cubic high / medium entropy alloys, Acta Mater 171 (2019) 201–215.

https://doi.org/10.1016/j.actamat.2019.04.017.
[46] Z. Wu, Y. Gao, H. Bei, Thermal activation mechanisms and Labusch-type strengthening analysis for a family of high-entropy and equiatomic solid-solution alloys, Acta Mater 120 (2016) 108–119. https://doi.org/10.1016/j.actamat.2016.08.047.
[47] T.B. Britton, F.P.E. Dunne, A.J. Wilkinson, On the mechanistic basis of deformation at the microscale in hexagonal close-packed metals, Proceedings of the Royal Society A: Mathematical, Physical and Engineering Sciences 471 (2015). https://doi.org/10.1098/rspa.2014.0881.

Fig. 1

Click here to access/download;Figure(s);Fig 1.tif



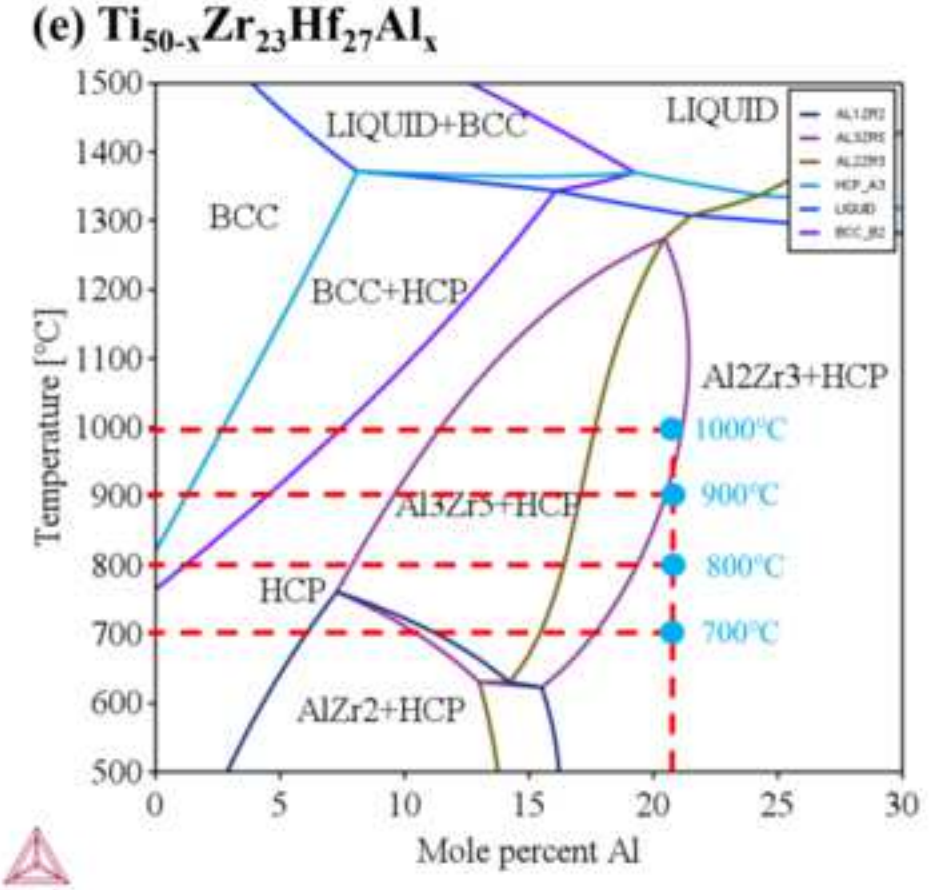


Fig.2

Click here to access/download;Figure(s);Fig.2.tif

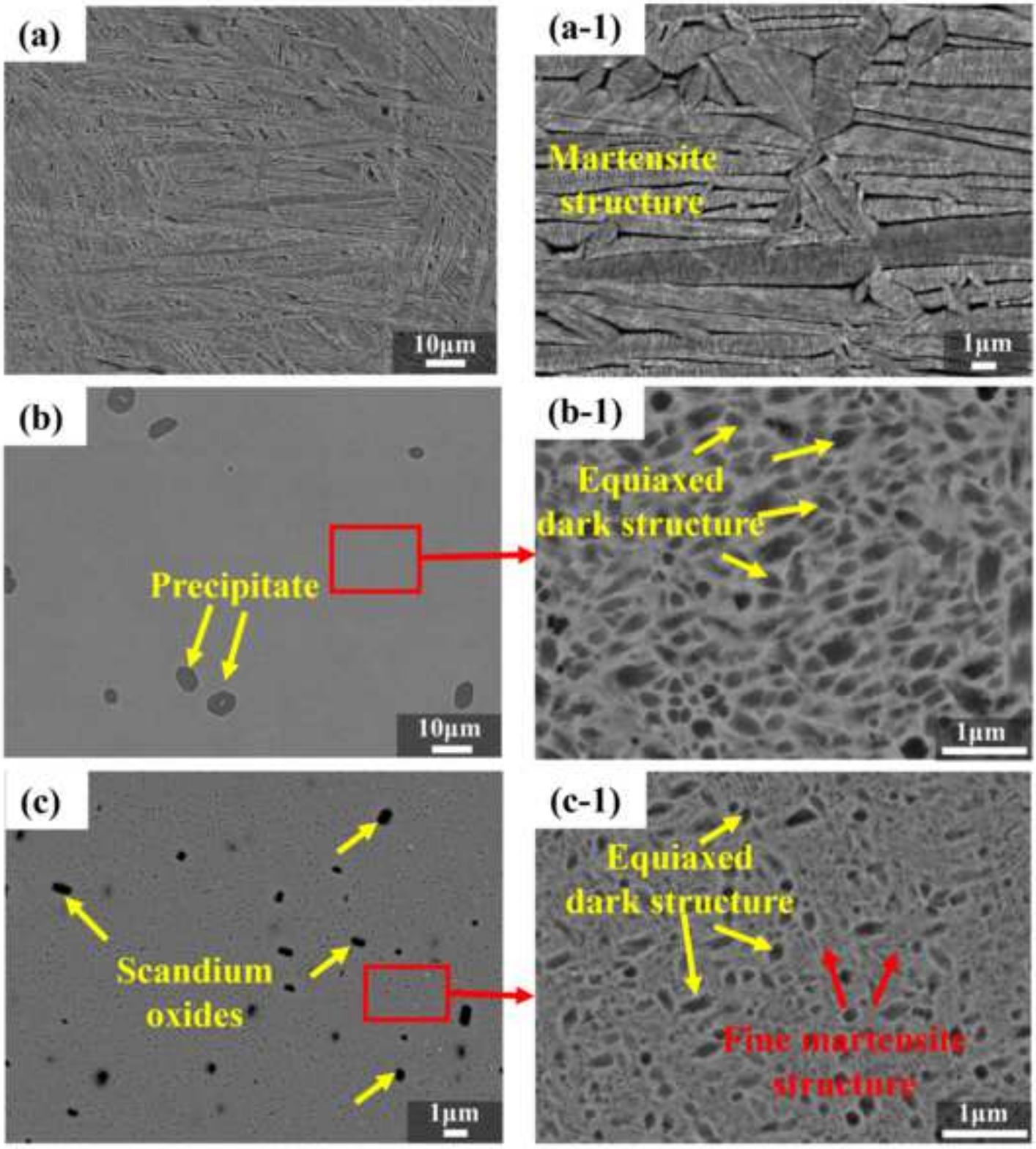


Fig.3

Click here to access/download;Figure(s);Fig.3.tif

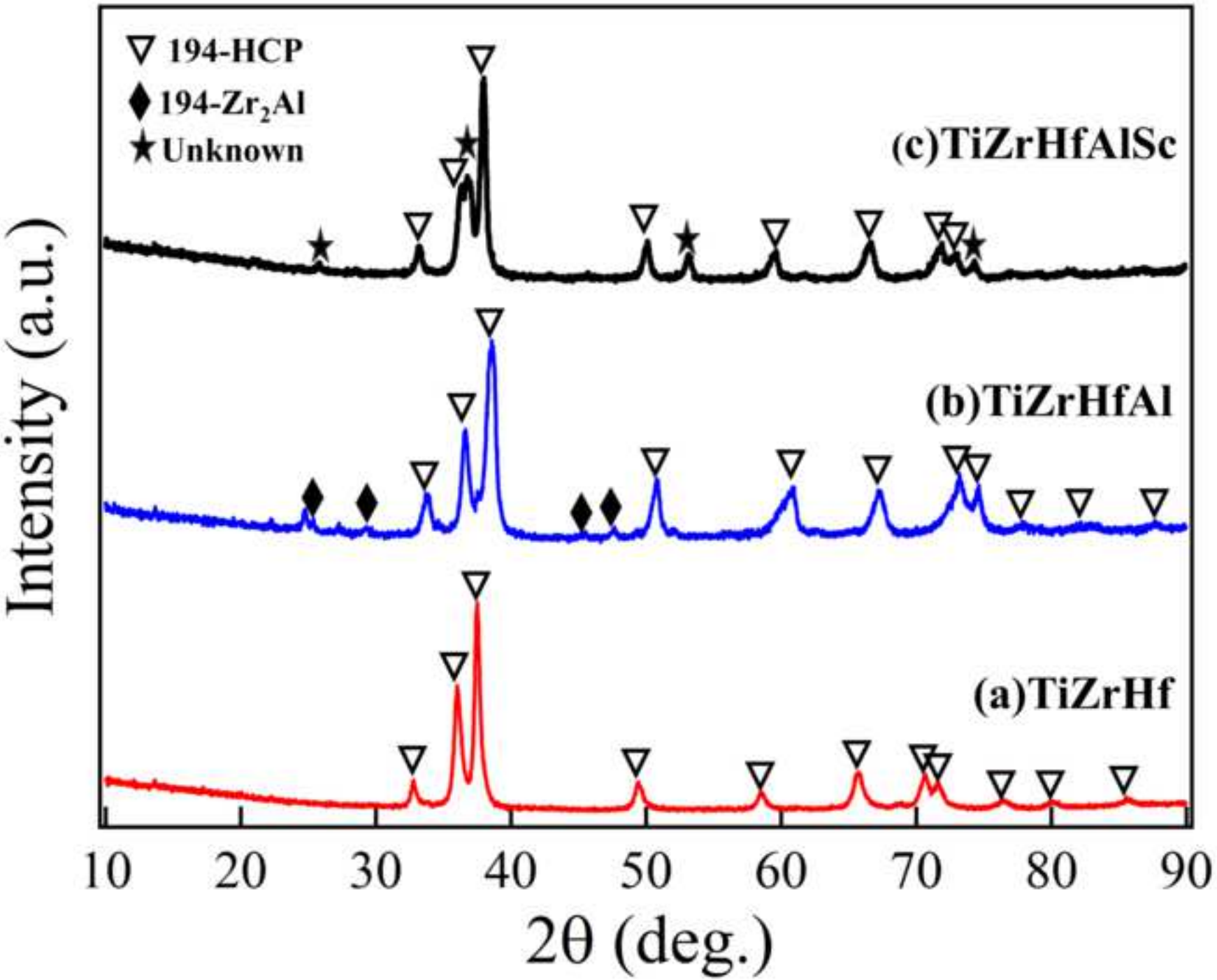


Fig.4

Click here to access/download;Figure(s);Fig.4.tif

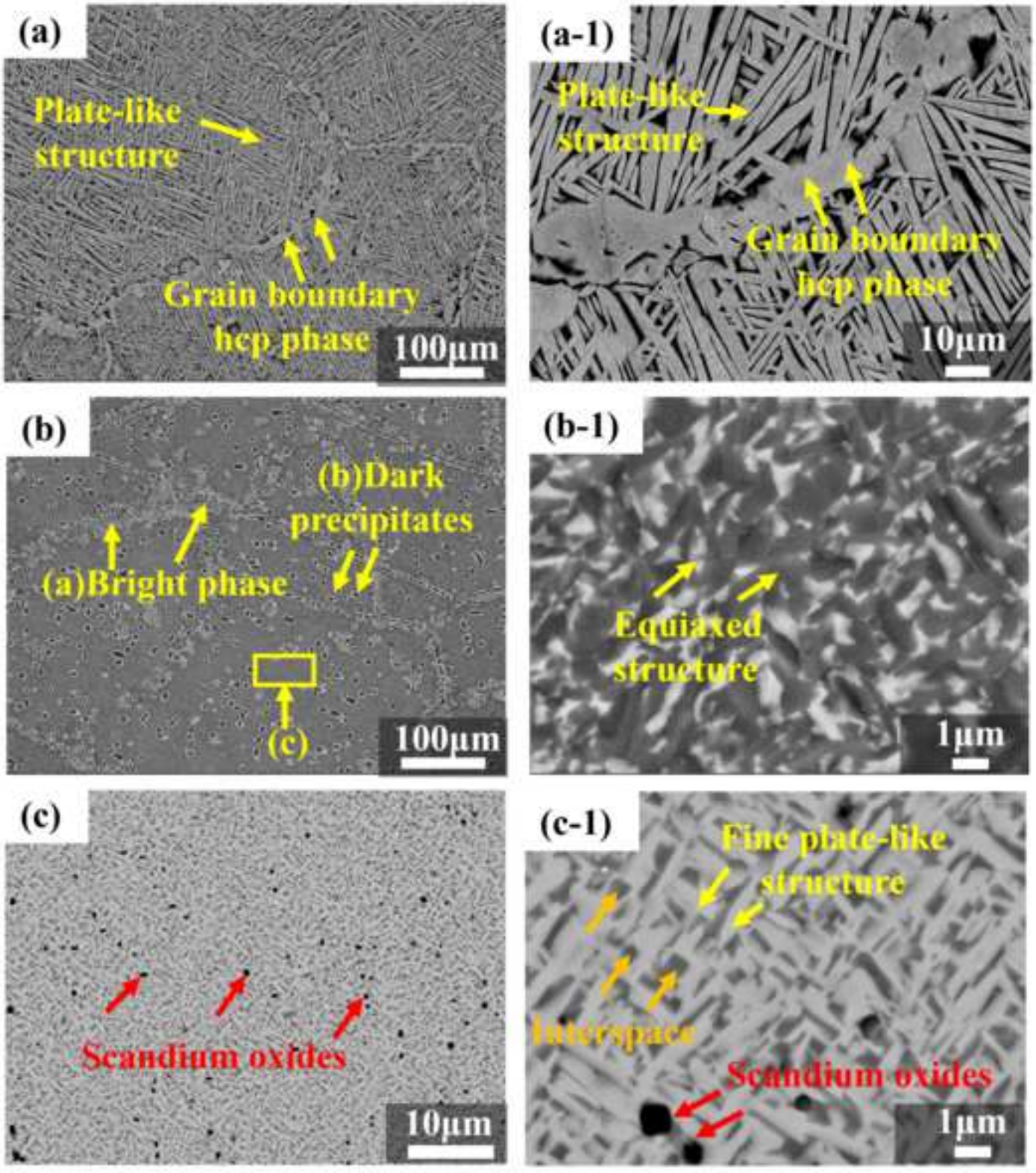


Fig. 5

Click here to access/download;Figure(s);Fig 5.tif

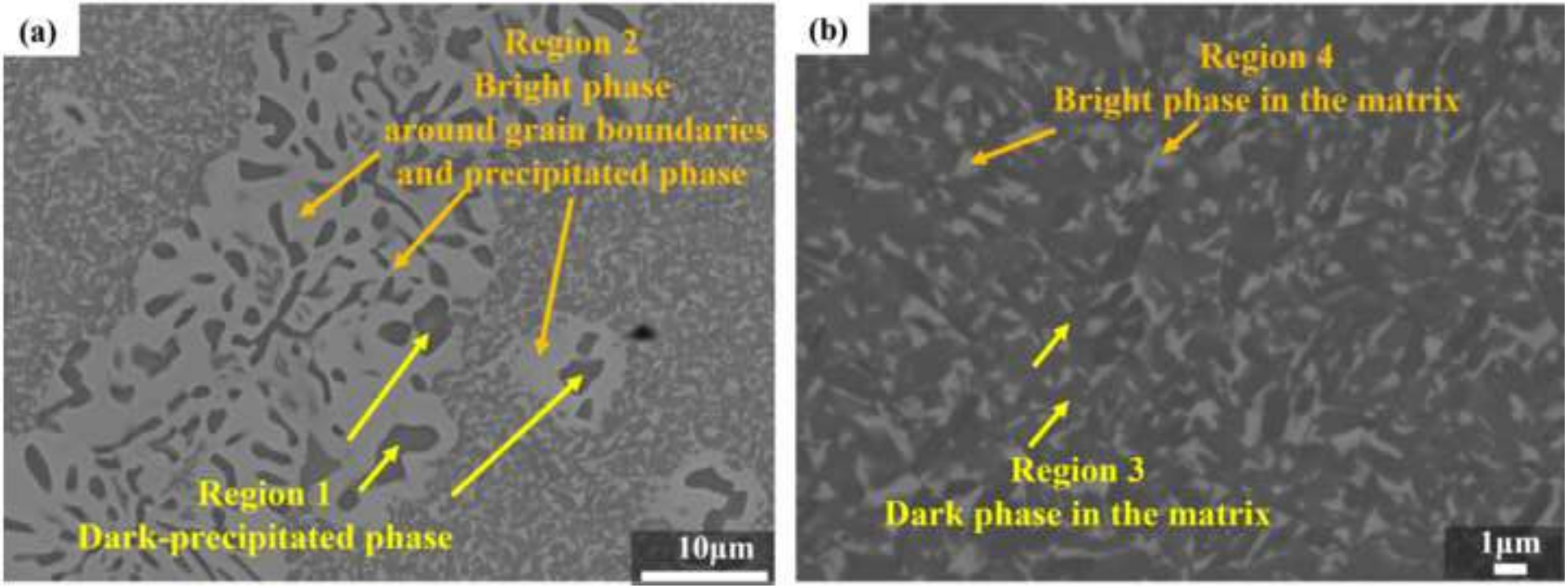


Fig. 6

Click here to access/download;Figure(s);Fig 6.tif

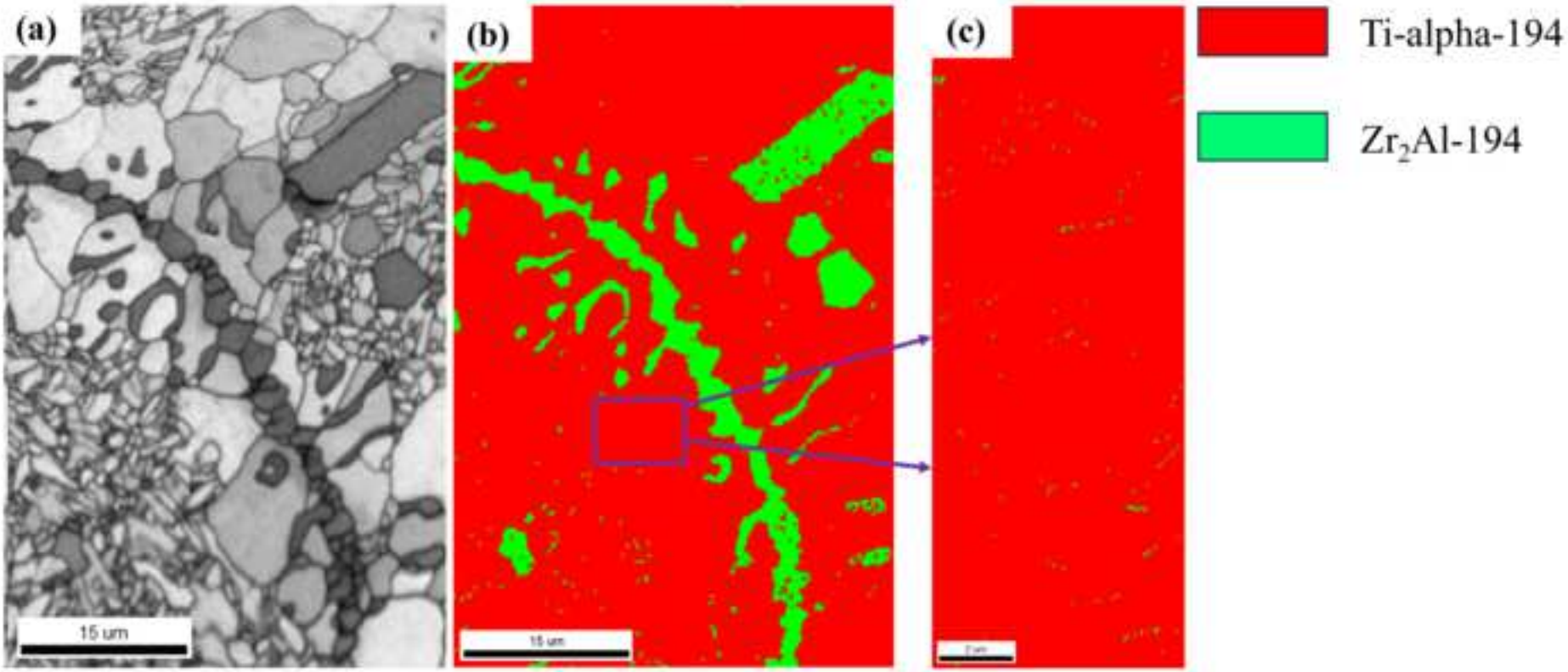


Fig. 7

Click here to access/download;Figure(s);Fig 7.tif

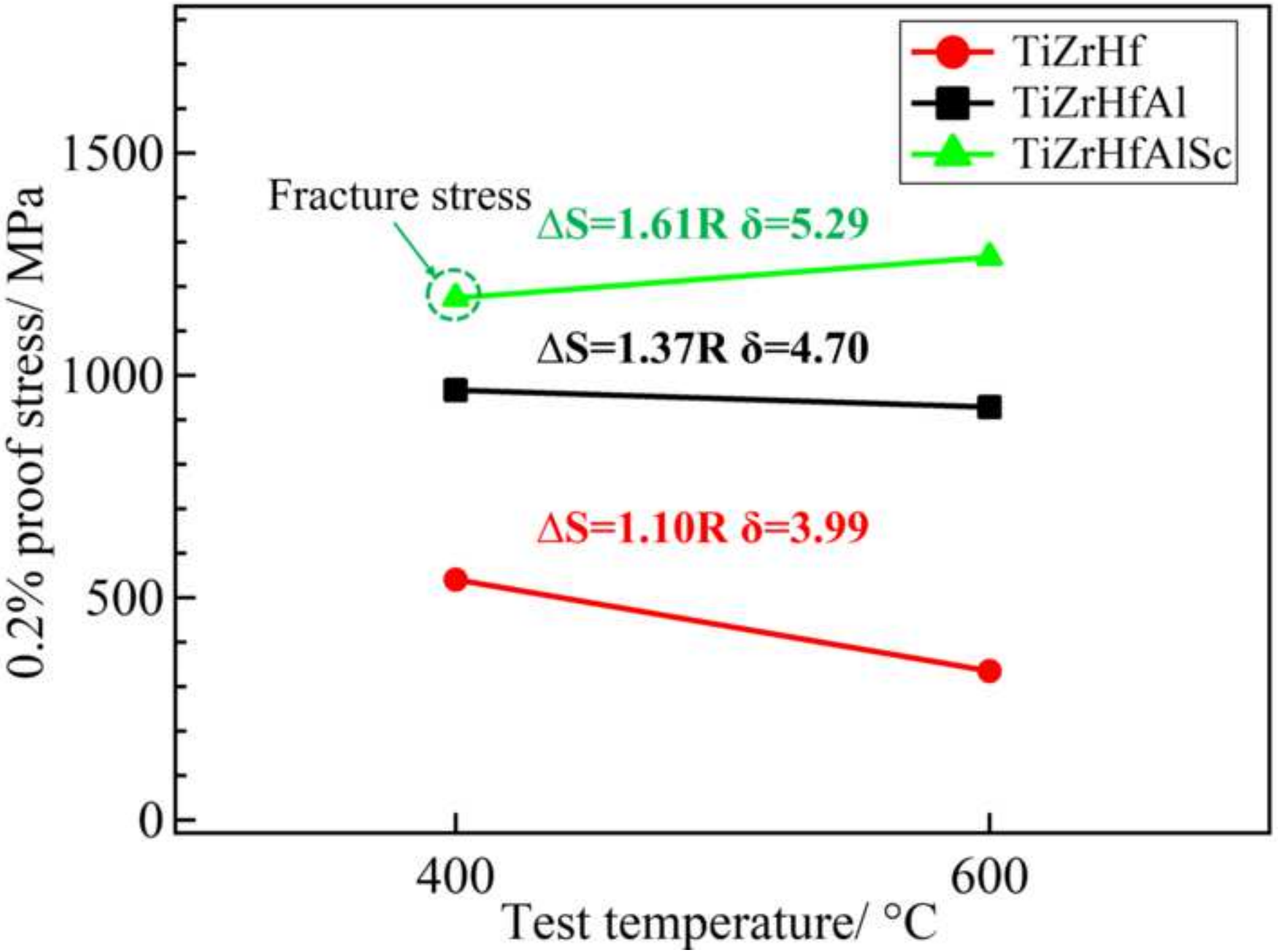


Fig. 8

Click here to access/download;Figure(s);Fig 8.tif

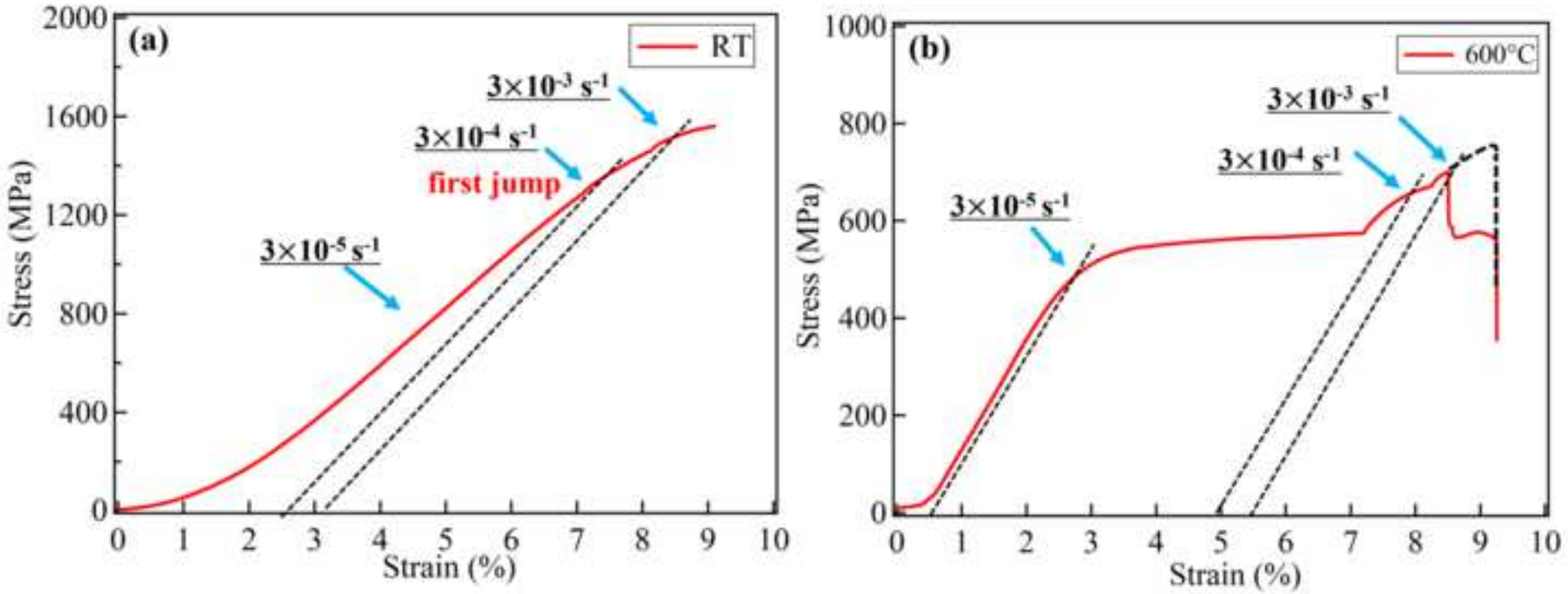
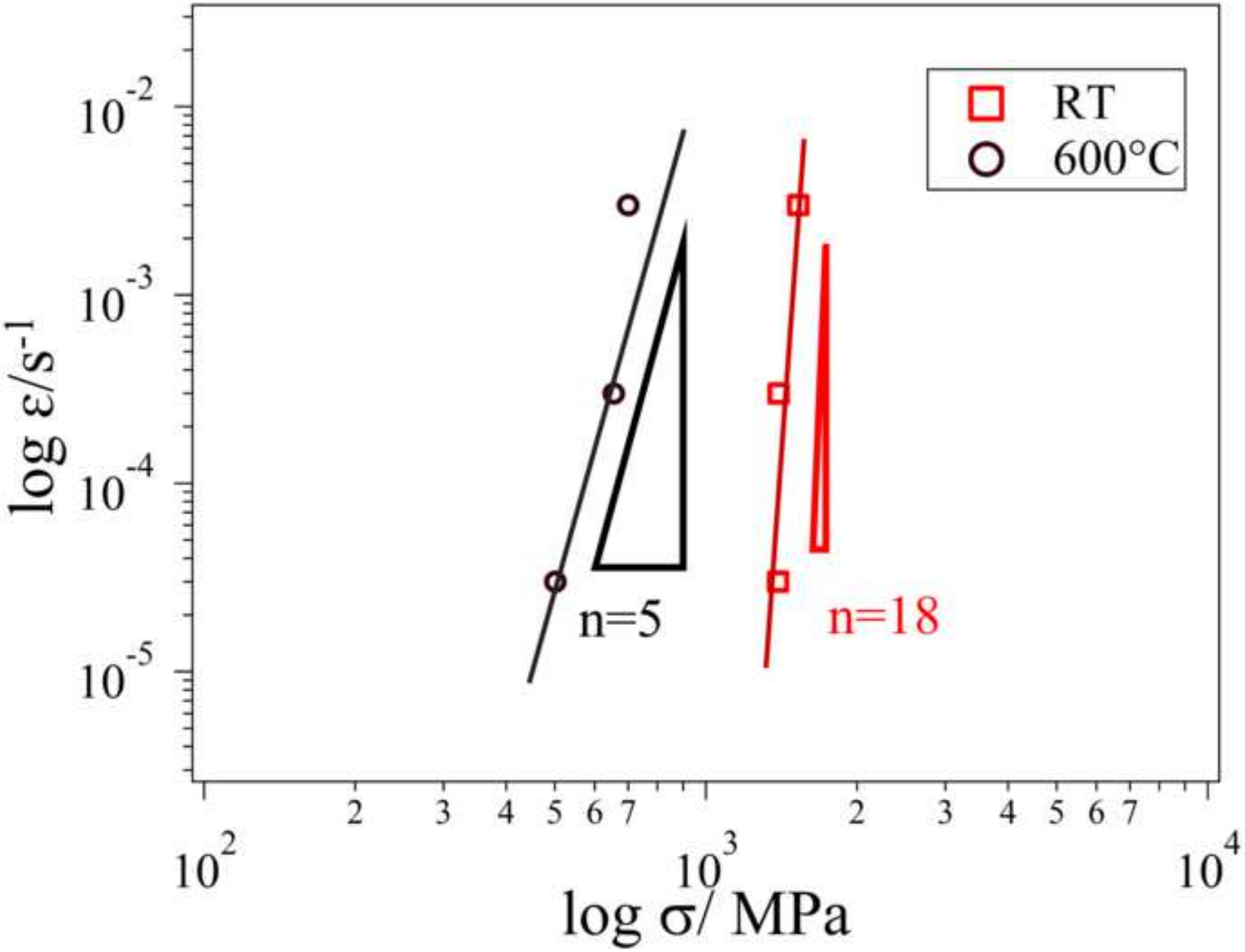


Fig. 9

Click here to access/download;Figure(s);Fig 9.tif



Highlights

- The equiaxed hcp phase was successfully formed in TiZrHfAl using the hot rolling process and subsequent heat treatment.
- The 0.2 % proof stress of TiZrHf, TiZrHfAl, and TiZrHfAlSc alloys at 400 and 600°C, increased with the increase of the average atomic size misfit δ and the mixing entropy ΔS_{mix}.
- The 0.2 % proof stress of TiZrHfAl with an equiaxed hcp structure at 400 and 600°C was significantly higher than conventional heat-resistant titanium alloys.
- The TiZrHfAl exhibits a high stress exponent of 18 and low activation volume at room temperature, suggesting a mechanism of strengthening with interruption of dislocation movement from minor obstacles such as atomic clusters or short-range orders in HEAs.

Declaration of interests

☒The authors declare that they have no known competing financial interests or personal relationships that could have appeared to influence the work reported in this paper.

☐The authors declare the following financial interests/personal relationships which may be considered as potential competing interests: